

This document is the accepted manuscript version of a published work that appeared in final form in Nano letters, copyright © American Chemical Society after peer review and technical editing by the publisher.

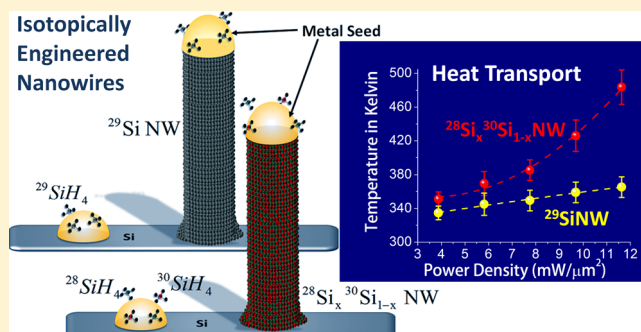
To access the final edited and published work see:  
<https://dx.doi.org/10.1021/acs.nanolett.5b00708>

Published under a “All rights reserved” license.

## 1 Phonon Engineering in Isotopically Disordered Silicon Nanowires

2 S. Mukherjee,<sup>†</sup> U. Givan,<sup>‡</sup> S. Senz,<sup>‡</sup> A. Bergeron,<sup>†</sup> S. Francoeur,<sup>†</sup> M. de la Mata,<sup>§</sup> J. Arbiol,<sup>§,||</sup>3 T. Sekiguchi,<sup>⊥</sup> K. M. Itoh,<sup>⊥</sup> D. Isheim,<sup>#</sup> D. N. Seidman,<sup>#</sup> and O. Moutanabbir<sup>\*,†</sup>4 <sup>†</sup>Department of Engineering Physics, Polytechnique Montréal, C. P. 6079, Succ. Centre-Ville, Montréal, Québec H3C 3A7, Canada5 <sup>‡</sup>Max Planck Institute of Microstructure Physics, Weinberg 2, D 06120 Halle (Saale), Germany6 <sup>§</sup>Institut de Ciencia de Materials de Barcelona, ICMAB-CSIC, Campus de la UAB, 08193 Bellaterra, Catalonia Spain7 <sup>||</sup>Institució Catalana de Recerca i Estudis Avançats (ICREA), 08010 Barcelona, Catalonia Spain8 <sup>⊥</sup>Department of Applied Physics and Physico-Informatics, Keio University, Hiyoshi, Yokohama, Japan9 <sup>#</sup>Department of Materials Science and Engineering Northwestern University Center for Atom-Probe Tomography, Northwestern  
10 University, Evanston, Illinois 60208-3108, United States11 **S** Supporting Information

12 **ABSTRACT:** The introduction of stable isotopes in the  
13 fabrication of semiconductor nanowires provides an additional  
14 degree of freedom to manipulate their basic properties, design  
15 an entirely new class of devices, and highlight subtle but  
16 important nanoscale and quantum phenomena. With this  
17 perspective, we report on phonon engineering in metal-  
18 catalyzed silicon nanowires with tailor-made isotopic composi-  
19 tions grown using isotopically enriched silane precursors  
20  $^{28}\text{SiH}_4$ ,  $^{29}\text{SiH}_4$ , and  $^{30}\text{SiH}_4$  with purity better than 99.9%. More  
21 specifically, isotopically mixed nanowires  $^{28}\text{Si}_x^{30}\text{Si}_{1-x}$  with a  
22 composition close to the highest mass disorder ( $x \sim 0.5$ ) were  
23 investigated. The effect of mass disorder on the phonon  
24 behavior was elucidated and compared to that in isotopically pure  $^{29}\text{Si}$  nanowires having a similar reduced mass. We found that  
25 the disorder-induced enhancement in phonon scattering in isotopically mixed nanowires is unexpectedly much more significant  
26 than in bulk crystals of close isotopic compositions. This effect is explained by a nonuniform distribution of  $^{28}\text{Si}$  and  $^{30}\text{Si}$  isotopes  
27 in the grown isotopically mixed nanowires with local compositions ranging from  $x = \sim 0.25$  to 0.70. Moreover, we also observed  
28 that upon heating phonons in  $^{28}\text{Si}_x^{30}\text{Si}_{1-x}$  nanowires behave remarkably differently from those in  $^{29}\text{Si}$  nanowires suggesting a  
29 reduced thermal conductivity induced by mass disorder. Using Raman nanothermometry, we found that the thermal conductivity  
30 of isotopically mixed  $^{28}\text{Si}_x^{30}\text{Si}_{1-x}$  nanowires is  $\sim 30\%$  lower than that of isotopically pure  $^{29}\text{Si}$  nanowires in agreement with  
31 theoretical predictions.

32 **KEYWORDS:** Nanowires, stable isotopes, phonons, thermal conductivity, Raman spectroscopy, atom probe tomography

33 **I**sotope engineering in semiconductors, which refers to  
34 controlling the content of each stable isotope within a  
35 lattice, has been a powerful paradigm to investigate and  
36 manipulate some of the important physical properties of  
37 semiconductors and exploit them in innovative device  
38 structures.<sup>1–13</sup> Isotopes of an element differ in the number of  
39 neutrons in the nucleus. This creates differences between the  
40 isotopes in their lattice dynamics and nuclear properties. For  
41 instance, the slight difference in zero point motion leads to a  
42 difference in atomic volume between the isotope atoms, which  
43 influences the lattice constant.<sup>3</sup> Also, the difference in  
44 electron–phonon coupling between crystals of different  
45 isotopic composition was found to affect the electronic band  
46 gap.<sup>4</sup> The nuclear spin is another significant difference between  
47 stable isotopes. For instance, natural silicon (Si) has three  
48 stable isotopes:  $^{28}\text{Si}$ ,  $^{29}\text{Si}$ , and  $^{30}\text{Si}$  with isotopic abundances of  
49 92.23, 4.67, and 3.10%, respectively. Among these three

isotopes, only  $^{29}\text{Si}$  has a nuclear spin of 1/2, whereas  $^{28}\text{Si}$  and  
50  $^{30}\text{Si}$  are nuclear spin-free. This property has been crucial in the  
51 realization of Si-based quantum information devices.<sup>5–8</sup> One of  
52 the most drastic isotope related effect in semiconductors is  
53 found in phonon properties.<sup>9–13</sup> Mass fluctuation induced by  
54 isotope disorder acts as a substitutional defect in a crystal thus  
55 affecting the phonon mean free path and consequently the  
56 phononic thermal conductivity. Measurements on isotopically  
57 pure Ge<sup>9</sup> and Si<sup>10</sup> crystals showed an enhanced thermal  
58 conductivity as compared to their natural counterparts. Also,  
59 lower thermal conductivity was recently demonstrated in Si  
60 isotope superlattices.<sup>11</sup> 61

Received: February 20, 2015

Revised: May 3, 2015

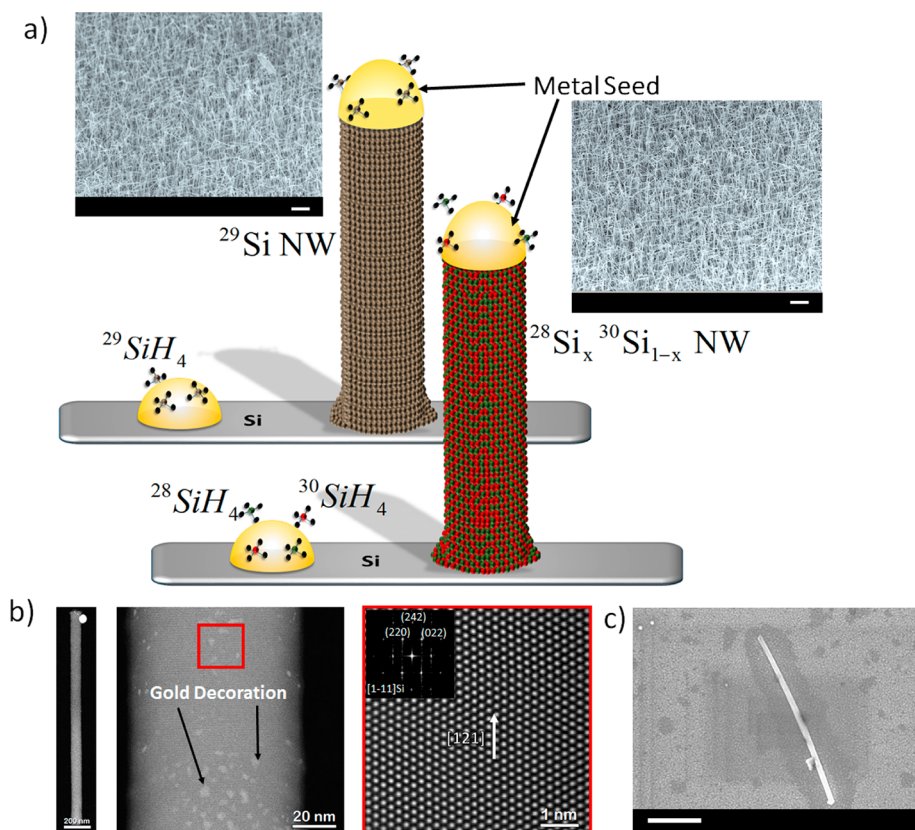


**Figure 1.** (a) A schematic illustration of the VLS growth of the isotopically engineered Si NWs. Vapor phase precursors are supplied to Au–Si eutectic droplet. For the isotopically pure NWs the precursor is  $^{29}\text{SiH}_4$  (purity 99.9%) and for the isotopically mixed NWs, a mixture of  $^{28}\text{SiH}_4$  (purity 99.99%) and  $^{30}\text{SiH}_4$  (purity 99.9%) was injected. Crystallization of Si atoms from the supersaturated droplet takes place at the droplet–nanowire interface which becomes the growth front. Inset: Low-magnification SEM images of as grown isotopically mixed  $^{28}\text{Si}_x^{30}\text{Si}_{1-x}$  NWs and isotopically pure  $^{29}\text{Si}$  NWs, both recorded at a tilt angle of  $60^\circ$ . The scale bars in both the figures denote 1  $\mu\text{m}$ . (b) STEM images of the isotopically pure  $^{29}\text{Si}$  NWs. Left: A single  $^{29}\text{Si}$  NW. The NW have grown along the [121] direction and the image taken from the [1 $\bar{1}$ 1] Si zone axis. The scale bar in the figure is 200 nm. Middle: STEM image of the NW sidewalls showing gold decoration on the facets. The scale bar in the figure is 20 nm. Right: High-magnification STEM image (taken from the region marked by the red box in the middle image) and the power spectrum (FFT) in the inset shows the high crystalline quality of the NW. The scale bar in the figure corresponds to 1 nm. (c) SEM image of a single  $^{29}\text{Si}$  NW after sonication and dispersion atop Au capped Si substrate. The scale bar denotes 1  $\mu\text{m}$ .

62 All the aforementioned properties of semiconductor stable  
 63 isotopes have been investigated and exploited in bulk materials  
 64 or thin films. Indeed, conspicuously missing are experimental  
 65 investigations of the influence of stable isotope impurities on  
 66 the basic characteristics of nanoscale materials despite the  
 67 crucial information they could provide concerning their  
 68 physical properties. Interestingly, there have been only a few  
 69 theoretical studies on the influence of the isotopic content on  
 70 basic phonon-related properties of Si nanowires (NWs).<sup>14,15</sup>  
 71 For instance, molecular dynamics (MD) simulations suggested  
 72 that the thermal conductivity of Si NWs is reduced  
 73 exponentially by isotopic impurities at room temperature.<sup>14,15</sup>  
 74 In the MD research, the simulated thermal conductivity of a  
 75  $^{28}\text{Si}_{0.5}^{29}\text{Si}_{0.5}$  NW yields  $\sim 80\%$  of that of isotopically pure  $^{28}\text{Si}$   
 76 NW. Also for a  $^{28}\text{Si}/^{29}\text{Si}$  multilayer NW with a 1.09 nm period,  
 77 the calculated thermal conductivity was found to be  $\sim 70\%$  of  
 78 that of isotopically pure  $^{28}\text{Si}$  NW.<sup>14</sup> Other calculations  
 79 demonstrate an improvement of more than 25% in thermo-  
 80 electric figure of merit of  $^{28}\text{Si}_{0.5}^{29}\text{Si}_{0.5}$  NWs as compared to a  
 81  $^{28}\text{Si}$  NWs.<sup>15</sup> No experiments have, however, been conducted to  
 82 elucidate these effects. With this perspective, we report in this  
 83 work the first experimental investigation of the influence of  
 84 isotope disorder on the phonon behavior in isotopically  
 85 engineered Si NWs.

The growth of NWs was carried out using the classical gold- 86  
 (Au) catalyzed vapor phase epitaxy using monoisotopic silane 87  
 $^{28}\text{SiH}_4$ ,  $^{29}\text{SiH}_4$ , and  $^{30}\text{SiH}_4$  with isotopic purity higher than 88  
 99.9%. These precursors were synthesized through the 89  
 hydrogenation of isotopically enriched  $\text{SiF}_4$ .<sup>16</sup> The growth 90  
 conditions are provided in the Supporting Information. Figure 91 f1  
 1a illustrates the schematics of the two sets of nanowires 92 f1  
 investigated in this work. The samples consist of isotopically 93  
 pure  $^{29}\text{Si}$  NWs and isotopically mixed  $^{28}\text{Si}_x^{30}\text{Si}_{1-x}$  NWs. The 94  
 former were grown by injecting the monoisotopic  $^{29}\text{SiH}_4$  95  
 precursor, whereas for the latter  $^{28}\text{SiH}_4$  and  $^{30}\text{SiH}_4$  were 96  
 simultaneously introduced in the growth chamber. The control 97  
 of the content of each isotope in the growing isotopically mixed 98  
 nanowires was achieved through the control of the partial 99  
 pressures of the two precursors. The low-magnification 100  
 scanning electron microscope (SEM) images (taken at a tilt 101  
 of  $60^\circ$ ) of the  $^{28}\text{Si}_x^{30}\text{Si}_{1-x}$  NWs and  $^{29}\text{Si}$  NWs are displayed in 102  
 the inset of Figure 1a. The grown NWs are typically 5  $\mu\text{m}$  long 103  
 with a diameter in the 30–100 nm range. Figure 1b shows the 104  
 scanning transmission electron microscope (STEM) image of a 105  
 $^{29}\text{Si}$  NW. The NW has grown in the [121] direction and the 106  
 image is taken from [1 $\bar{1}$ 1] Si zone axis. The SEM analysis 107  
 indicates that while the majority of  $^{29}\text{Si}$  NWs have grown along 108  
 the [111] direction a few have actually grown at an angle of 109

110  $\sim 19.5^\circ$  with respect to the [111] direction corresponding to  
 111 the [121] crystallographic direction. It is noticeable that the  
 112 NW surface is decorated with Au clusters mainly near the tip of  
 113 the NW. This is attributed to Au diffusion from the catalyst  
 114 droplet along the NW sidewalls during the quenching to room  
 115 temperature after growth interruption.<sup>17,18</sup> The high-magnifica-  
 116 tion STEM image of the NW included in Figure 1b and the  
 117 power spectrum (fast Fourier transform (FFT)) in the inset  
 118 show that the grown NWs are of the highest crystalline quality.  
 119 The STEM analysis of the  $^{28}\text{Si}_x^{30}\text{Si}_{1-x}$  NWs (not shown here)  
 120 confirms that the two sets of NWs have identical structural and  
 121 morphological properties.

122 Raman spectroscopy was employed to investigate the  
 123 vibrational properties of these NWs. To enable the analysis  
 124 of individual NWs, the as-grown NWs were first transferred  
 125 onto Au-capped Si to suppress the background signal from the  
 126 underlying substrate during subsequent Raman analysis.  
 127 Backscattering micro-Raman experiments were carried using  
 128 two laser lines 488 nm (low power measurements) and 514 nm  
 129 (high power measurements) at incident power densities in the  
 130 range of 0.08–17.76  $\text{mW}/\mu\text{m}^2$  (see Supporting Information for  
 131 more details). The average length of the NWs after dispersion  
 132 on Au was found to be on the order of 2–3  $\mu\text{m}$ . All Raman  
 133 measurements were performed on single NWs that are in an  
 134 excellent thermal contact with Au layer (Figure 1c). Clustered  
 135 and suspended NWs were avoided in this analysis as they heat  
 136 up faster when exposed to laser beam, which influences their  
 137 Raman modes.<sup>19</sup> Figure 2 shows the Si–Si LO phonon spectra

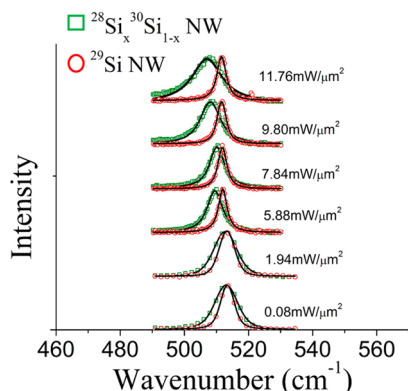


**Figure 2.** Si–Si LO normalized phonon spectra of  $^{28}\text{Si}_x^{30}\text{Si}_{1-x}$  NW and  $^{29}\text{Si}$  NW at different incident laser power densities. The spectra at 1.94 and 0.08  $\text{mW}/\mu\text{m}^2$  were recorded using the 488 nm laser and the remaining spectra using the 532 nm laser. The spectra shown here are representative of a single  $^{28}\text{Si}_x^{30}\text{Si}_{1-x}$  NW and a single  $^{29}\text{Si}$  NW. The data points for the  $^{28}\text{Si}_x^{30}\text{Si}_{1-x}$  NWs are shown as empty green squares and that of  $^{29}\text{Si}$  NWs correspond to empty red circles. The black continuous curve corresponds to the Voigt fit.

138 of single  $^{28}\text{Si}_x^{30}\text{Si}_{1-x}$  and  $^{29}\text{Si}$  NWs at different incident laser  
 139 power densities. A detailed comparison of Raman spectra of  
 140  $^{28}\text{Si}_x^{30}\text{Si}_{1-x}$  and  $^{29}\text{Si}$  single NWs at low power regime is  
 141 provided in Figure S1 (Supporting Information). Note that all  
 142 effects related to phonon confinement are excluded here as the  
 143 diameter of the investigated NWs is larger than the phonon  
 144 mean free path in Si around room temperature. Recorded  
 145 spectra were fitted with Voigt line profiles to extract peak  
 146 positions and full width at half-maximum (fwhm).

147 A first analysis of the data is based on the quasi-harmonic  
 148 approximation, which is a valid approximation for semi-

conductors at room temperature.<sup>20</sup> Herein, it is important to  
 minimize the excess local heating of the NWs, which would  
 occur when the incident laser power is sufficiently high. Hence,  
 all calculations involving the quasi-harmonic approximation  
 were carried out on data sets recorded at the lowest incident  
 power density of 0.08  $\text{mW}/\mu\text{m}^2$  at which the local temperature  
 of the NWs is confirmed to be equal to the ambient  
 temperature of 300 K (Supporting Information). A close  
 inspection of the spectra exhibited in Figure 2 shows two  
 separate phonon related effects. First, at all incident laser  
 powers the Raman spectrum for  $^{28}\text{Si}_x^{30}\text{Si}_{1-x}$  NWs is always  
 broader and red-shifted as compared to the spectrum of  $^{29}\text{Si}$   
 NWs. Second, regardless of the type of the NW, as the incident  
 power increases, all peaks broaden and redshift. This effect is  
 due to laser-induced heating of the NWs. Figure 3 depicts the  
 evolution of the average peak position and the evolution of the  
 average fwhm with incident power density for both  $^{28}\text{Si}_x^{30}\text{Si}_{1-x}$   
 and  $^{29}\text{Si}$  NWs. In Figure 3a,b are displayed the data recorded at  
 low laser power densities averaged over a large number (>10 of  
 single NWs). High-power measurements are given in Figure  
 3d,e. The peak position and fwhm of 4–5 individual  $^{28}\text{Si}_x^{30}\text{Si}_{1-x}$   
 NWs and  $^{29}\text{Si}$  NWs, as extracted from the Voigt fit of the raw  
 data, at both low and high power levels are displayed in Figure  
 S2 (Supporting Information). Interestingly, both the broad-  
 ening and the redshift are found to be more pronounced for  
 $^{28}\text{Si}_x^{30}\text{Si}_{1-x}$  NWs. For instance, the average peak position within  
 the laser power range investigated varies by about 4  $\text{cm}^{-1}$  for  
 $^{28}\text{Si}_x^{30}\text{Si}_{1-x}$  NWs as compared to  $\sim 1 \text{ cm}^{-1}$  for  $^{29}\text{Si}$  NWs. This  
 indicates that the two types of NWs react differently to local  
 heating induced by laser.

In the following, we elucidate the origin of the remarkable  
 changes in Raman spectra as a function of the NW isotopic  
 content. According to the virtual crystal approximations  
 (VCA), a simple harmonic analysis predicts that the energy  
 of a phonon mode is inversely proportional to the square root  
 of the average isotopic mass<sup>1</sup>  $-\omega_{\text{phonon}} \propto (1/\langle m \rangle)^{1/2}$ . Here  $m$   
 is the average isotopic mass given by  $\langle m \rangle = \sum_i c_i m_i$ , with  $c_i$   
 being the fractional composition of an isotope of mass  $m_i$ . Using the  
 ratio of the average peak position at the lowest incident power  
 density of 0.08  $\text{mW}/\mu\text{m}^2$  (Figure 3a) and the value of  $\langle m \rangle_{^{29}\text{Si}}$   
 we computed  $\langle m \rangle_{\text{Iso-mix}} = 29.05$  amu. Thus, the corresponding  
 fractional composition of  $^{28}\text{Si}$  in the isotopically mixed NWs is  
 $x = 0.47 \pm 0.07$  calculated from the known values of  $\langle m \rangle_{^{28}\text{Si}}$   
 and  $\langle m \rangle_{^{30}\text{Si}}$  in the identity:  $\langle m \rangle_{\text{Iso-mix}} = x \times \langle m \rangle_{^{28}\text{Si}} + (1 - x)$   
 $\times \langle m \rangle_{^{30}\text{Si}}$ . Note that composition calculated employing the  
 quasi-harmonic approximation is always an average estimate.

In Figure 3a, the shift rate of the average peak position with  
 power density up to 5–6  $\text{mW}/\mu\text{m}^2$  is only slightly higher for  
 $^{28}\text{Si}_x^{30}\text{Si}_{1-x}$  NWs as compared to  $^{29}\text{Si}$  NWs (the corresponding  
 slopes of the dotted lines are 0.38 and 0.30  $(\text{cm}^{-1}\mu\text{m}^2)/(\text{mW})$ ,  
 respectively). At higher power densities, the behavior of  
 $^{28}\text{Si}_x^{30}\text{Si}_{1-x}$  NWs is markedly different from  $^{29}\text{Si}$  NWs with  
 the average phonon frequency of the former undergoing a  
 drastic redshift as compared to the latter (Figure 3d). The  
 evolution of fwhm follows the same trend as the shift in  
 phonon frequency. Below  $\sim 6 \text{ mW}/\mu\text{m}^2$ , the average fwhm of  
 $^{28}\text{Si}_x^{30}\text{Si}_{1-x}$  NWs and  $^{29}\text{Si}$  NWs evolve qualitatively similarly  
 with incident power density. At all incident power densities the  
 spectra of  $^{28}\text{Si}_x^{30}\text{Si}_{1-x}$  NWs are always broader than that of  $^{29}\text{Si}$   
 NWs. This can be also verified from the respective spectra  
 displayed in Figure 2. At low and mid power ranges, the average  
 fwhm of the former is about 3–3.5  $\text{cm}^{-1}$  broader than the

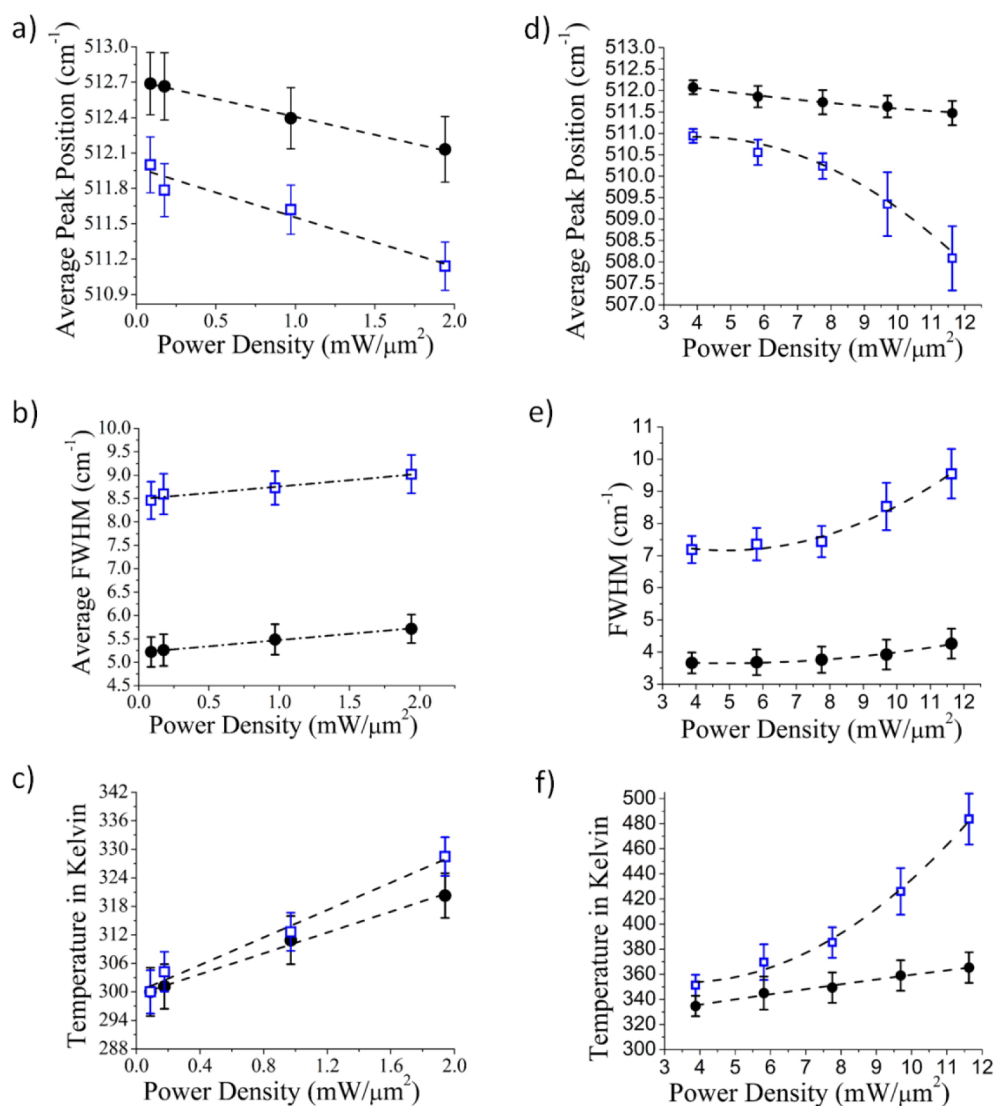


**Figure 3.** (a,b) Measurements using 488 nm laser at low incident power density; (d,e) measurements using 532 nm laser at high incident power density. In all figures, the empty blue squares correspond to the isotopically mixed  $^{28}\text{Si}_x^{30}\text{Si}_{1-x}$  NWs and the filled black circles represent the isotopically pure  $^{29}\text{Si}$  NWs. (a,d) Evolution of average peak position with incident laser power density for both  $^{28}\text{Si}_x^{30}\text{Si}_{1-x}$  NWs and  $^{29}\text{Si}$  NWs. (b,e) Evolution of the average fwhm with incident laser power density for both  $^{28}\text{Si}_x^{30}\text{Si}_{1-x}$  NWs and  $^{29}\text{Si}$  NWs. In panels a and b, the averaging was done over measurements on more than 10 single NWs, and in panels d and e the averaging was done over measurements on 7 single NWs. The error bars in panels a, b, d, and e are double the standard deviation of the peak position and fwhm from respective average values. (c,f) Plots of the effective local temperature of the NWs extracted from the shift in average peak position in panels a and d, respectively. The error bars represent the uncertainty in the calculated temperature due to the standard deviation of the measured peak position. The dotted lines in panels a–f are guides to the eye.

211 latter. A detailed discussion on the origin of this effect will be  
 212 presented later in the text. As it can be seen in Figure 3e, at  
 213 high power regime the spectra of  $^{28}\text{Si}_x^{30}\text{Si}_{1-x}$  NWs start to  
 214 broaden much rapidly as compared to  $^{29}\text{Si}$  NWs. The difference  
 215 in absolute values of the average fwhm between Figure 3, panels  
 216 b and e, comes simply from the difference in spectral resolution  
 217 between the two setups (Supporting Information).

218 The redshift in peak position and broadening of Raman  
 219 spectra with increasing power densities are indicative of how  
 220 the NWs are reacting to laser-induced heating. From Figure 3,  
 221 it can be seen that the behavior of the two types of NWs only  
 222 show slight differences at low power, but at high power  
 223  $^{28}\text{Si}_x^{30}\text{Si}_{1-x}$  NWs are much more affected than  $^{29}\text{Si}$  NWs. A  
 224 convenient way to quantify this heating effect is to extract the  
 225 NW local temperature. Herein, an estimate of the effective local

temperature is made from the shift in average peak position 226  
 with the incident laser power. The peak position of a NW, 227  
 $\Omega(T)$  at a temperature “ $T$ ”, is given by<sup>21</sup>  $\Omega(T) = \omega_0 + \Pi(T)$ , 228  
 where  $\omega_0$  is the peak position at 0 K and  $\Pi(T)$  is the shift of 229  
 peak position at  $T$ , given by 230

$$\Pi(T) = C \left[ 1 + \frac{2}{e^{\hbar\omega_0/2k_B T} - 1} \right] + D \left[ 1 + \frac{3}{e^{\hbar\omega_0/3k_B T} - 1} + \frac{3}{(e^{\hbar\omega_0/2k_B T} - 1)^2} \right] \quad (1) \quad 231$$

where “ $C$ ” and “ $D$ ” are constants. The first term is related to 232  
 three-phonon anharmonic interaction and the second term 233  
 represents the four phonon interaction. The probability of the 234  
 latter being small, we can reasonably neglect it to be left with 235  
 the first term in the right-hand side of (1). Balkanski et al. 236

237 calculated the phonon frequency for  $^{Nat}Si$  at 0 K,  $\omega_0^{Nat-Si} =$   
 238  $529 \text{ cm}^{-1}$  (using only the three phonon process). By taking into  
 239 account the change in the reduced mass, we calculate  $\omega_0^{Iso-mix}$   
 240 (for  $^{28}Si_x^{30}Si_{1-x}$  NWs) and  $\omega_0^{29-Si}$  (for  $^{29}Si$  NWs) to be 519.80  
 241 and  $520.81 \text{ cm}^{-1}$ , respectively.  $C$  was estimated from the data  
 242 recorded at the lowest laser power density ( $0.08 \text{ mW}/\mu\text{m}^2$ )  
 243 corresponding to a temperature of 300 K. Next,  $\prod(T)$  was  
 244 calculated from Figure 3a,b for different incident power  
 245 densities and the NW local temperature was then estimated  
 246 as displayed in Figure 3c,f. The plot reveals that  $^{28}Si_x^{30}Si_{1-x}$   
 247 NWs are getting slightly more heated up as compared to  $^{29}Si$   
 248 NWs in the low power density regime ( $<6 \text{ mW}/\text{cm}^2$ ), the  
 249 temperature of the former is higher by  $\sim 10\text{--}15 \text{ K}$  at  $1.94 \text{ mW}/$   
 250  $\mu\text{m}^2$  and  $\sim 25\text{--}30 \text{ K}$  at  $5.88 \text{ mW}/\mu\text{m}^2$  as compared to the latter.  
 251 However, at the highest power of  $11.76 \text{ mW}/\mu\text{m}^2$  the  
 252 difference in temperatures is quite significant. Indeed, the  
 253 temperature of  $^{28}Si_x^{30}Si_{1-x}$  NWs is almost 120 K higher than  
 254 that of  $^{29}Si$  NWs. At low power regime, the rate of increase of  
 255 temperature with increasing laser power,  $\Delta T/\Delta P$ , is  $\sim 1.30$   
 256 times higher for  $^{28}Si_x^{30}Si_{1-x}$  NWs than  $^{29}Si$  NWs and becomes  
 257  $\sim 6$  times larger in the high power regime ( $6\text{--}12 \text{ mW}/\mu\text{m}^2$ ).

258 To evaluate the change in thermal conductivity between the  
 259 two sets of NWs, which led to the result described above, we  
 260 used Raman nanothermometry<sup>22,23</sup> in conjunction with a heat  
 261 transport model. This model draws its basis from the  
 262 assumptions that the region of the NW exposed to laser acts  
 263 as the heat source and that the major portion of the generated  
 264 heat is dissipated by conduction along the NW growth axis and  
 265 at the NW-Au interface (Supporting Information Figure S3).  
 266 Details of the model are provided in the Supporting  
 267 Information. Around 300 K, based on the rate of increase of  
 268 temperature, we estimated the ratio of thermal conductivities of  
 269  $^{29}Si$  NWs to  $^{28}Si_x^{30}Si_{1-x}$  NWs  $\kappa_{Si-29}/\kappa_{Iso-Mix}$  to be  $\sim 1.30$ . This  
 270 means there is a  $\sim 30\%$  decrease in  $\kappa_{Iso-Mix}$  as compared to  
 271  $\kappa_{Si-29}$ . Interestingly, this value is close to the theoretical  
 272 prediction of 30% reduction in case of  $^{28}Si_{0.5}^{30}Si_{0.5}$  bulk alloys as  
 273 compared to  $^{Nat}Si$  at room temperature,<sup>24</sup> but it is slightly  
 274 higher than  $\sim 20\%$  reduction predicted for  $^{28}Si_{0.5}^{29}Si_{0.5}$  NW as  
 275 compared to  $^{28}Si$  NW at 300 K.<sup>14</sup> It is also noteworthy that the  
 276 observed mass disorder-induced change in Si NW thermal  
 277 conductivity is lower the 50% reduction demonstrated for  
 278  $^{12}C_{0.5}^{13}C_{0.5}$  graphene as compared to purified  $^{13}C$  graphene.<sup>25</sup>  
 279 For Si NWs, Yang and co-workers predicted that at room  
 280 temperature a much significant reduction in thermal con-  
 281 ductivity up to  $\sim 70\%$  can be achieved when a  $^{28}Si$  NW is mixed  
 282 at 50% with  $^{42}Si$  atoms.<sup>14</sup> However,  $^{42}Si$  being radioactive with  
 283 a half-life of  $\sim 13 \text{ ms}$  cannot obviously be implemented for any  
 284 practical purpose. Note that the ratio of thermal conductivity  
 285 was specifically calculated in the low power regime because the  
 286 fluctuations in the measured peak position of different  
 287  $^{28}Si_x^{30}Si_{1-x}$  NWs at high power regime are very large  
 288 (Supporting Information Figure S2:Ab) thus making the  
 289 estimation of the temperature of  $^{28}Si_x^{30}Si_{1-x}$  NWs fraught  
 290 with large uncertainties.

291 Although our experimental data are consistent with early  
 292 theoretical predictions, isotope mixing alone cannot explain all  
 293 the observed differences in phonon properties between  
 294 isotopically disordered and pure NWs. In Figure 3b, the  
 295 fwhm of  $^{28}Si_x^{30}Si_{1-x}$  NWs is consistently larger by almost 3–3.5  
 296  $\text{cm}^{-1}$  at all incident power compared to the  $^{29}Si$  NWs. As  
 297 phonon confinement is excluded here, broadening of a Raman  
 298 spectrum occurs due to scattering of phonons. In general, the

greater the broadening of a Raman line, the greater is the rate of 299  
 phonon scattering in the material. At a first glance, it appears 300  
 that excess broadening is due to the sole effect of scattering of 301  
 phonons from the mass disorder but our analysis suggests that 302  
 this contribution alone is not sufficient. Herein, in order to 303  
 quantify the effect of mass disorder we first compare our data 304  
 with the results of Raman measurements on isotopically 305  
 engineered bulk samples.<sup>26</sup> In those studies, Cardona and co- 306  
 workers measured bulk Si samples of different isotopic 307  
 composition. The Raman spectra of a material has a slight 308  
 dependence on the excitation wavelength<sup>27</sup> but at low 309  
 incidence power this dependence can be neglected. We focus 310  
 mainly on bulk  $^{28}Si_{0.5}^{30}Si_{0.5}$  sample as it has almost the same 311  
 average isotopic composition as our isotopically mixed NWs 312  
 and hence nearly the same mass variance,  $g_2$ , which is given by 313

$$g_2 = \frac{\sum_i c_i m_i^2 - (\sum_i c_i m_i)^2}{(\sum_i c_i m_i)^2} = \frac{\langle m^2 \rangle - \langle m \rangle^2}{\langle m \rangle^2} \quad (2) \quad 314$$

There are various scattering mechanisms for phonons in a 315  
 material. The first is the anharmonic scattering of a LO zone- 316  
 center phonon into two or three phonons with larger wave 317  
 vector and smaller energy. Anharmonic scattering increases 318  
 with temperature and at a given temperature the rate of 319  
 anharmonic scattering of phonons is inversely proportional to 320  
 the average isotopic mass.<sup>26</sup> The second is the isotope 321  
 scattering of phonons that is proportional to  $g_2$ .<sup>28</sup> The third 322  
 is the Umklapp scattering of two phonons, which produces a 323  
 third phonon outside the first Brillouin zone. Umklapp 324  
 scattering becomes important for temperatures above the 325  
 Debye temperature, which is 645 K for Si.<sup>29</sup> Thus, this 326  
 scattering is irrelevant in our case as the temperature of the 327  
 analyzed NWs remains significantly below this temperature 328  
 (Figure 3). The fourth is the surface scattering of phonons, 329  
 which is also temperature independent but depends inversely 330  
 on the size of the material under consideration.<sup>30</sup> Surface 331  
 scattering can be neglected for bulk materials but not for NWs. 332  
 The fifth is the Fano scattering, which is the scattering of 333  
 phonons from thermally generated electron hole pairs.<sup>31</sup> 334  
 Because Fano scattering is significant only at high levels of 335  
 carrier injection, it can be neglected for intrinsic Si NWs 336  
 investigated in this work. This leaves us with just two scattering 337  
 mechanisms in bulk samples, the anharmonic scattering and 338  
 scattering from isotope disorder. We extracted from ref 26 that 339  
 for the bulk  $^{28}Si_{0.5}^{30}Si_{0.5}$  sample,  $\Delta_{Anhrm}^{Iso-Mix \text{ Bulk}}$ , the contribution 340  
 of anharmonic scattering of phonons and  $\Delta_{Isotope}^{Iso \text{ Mix Bulk}}$ , the 341  
 contribution of isotope scattering of phonons to the total line 342  
 broadening at  $T = 6 \text{ K}$  are about 1.16 and  $0.065 \text{ cm}^{-1}$ , 343  
 respectively. We extrapolated  $\Delta_{Anhrm}^{Iso-Mix \text{ Bulk}}$  to  $T = 300 \text{ K}$ , using 344  
 the following equation<sup>21</sup> 345

$$\Delta_{Anhrm}(T) = A \left[ 1 + \frac{2}{e^{\hbar\omega_0/2k_B T} - 1} \right] \quad (3) \quad 346$$

Similar to eq 1 we have neglected the four phonon 347  
 interaction and normalized the data for  $\Delta_{Anhrm}^{Iso-Mix \text{ Bulk}}$  at  $T = 6$  348  
 K to find the constant “A”.  $\omega_0$  for the bulk  $^{28}Si_{0.5}^{30}Si_{0.5}$  sample 349  
 was calculated by the same approach used to calculate  $\omega_0^{Iso-Mix}$  350  
 and  $\omega_0^{29-Si}$ . We found  $\Delta_{Anhrm}^{Iso-Mix \text{ Bulk}}$  ( $T = 300 \text{ K}$ ) =  $1.36 \text{ cm}^{-1}$ . 351  
 The difference in spectral resolution between our setup and the 352  
 setup used in ref 26 is accounted for in this analysis.<sup>32,33</sup> 353  
 Summing up the discussion in form of equations, the fwhm of 354  
 bulk  $^{28}Si_{0.5}^{30}Si_{0.5}$  sample consists of two contributions 355

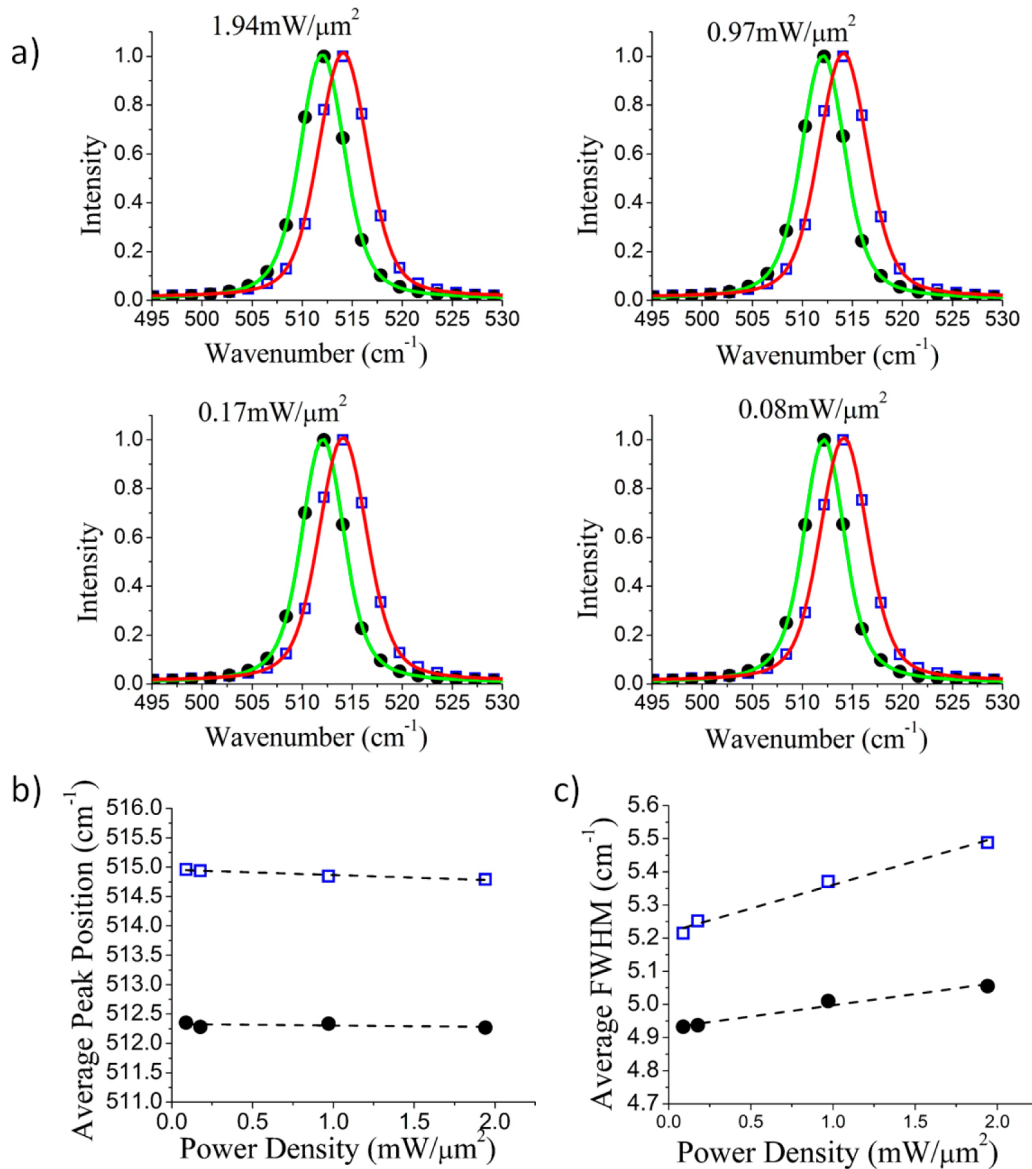


**Figure 4.** (a) Si-Si LO normalized phonon spectra of  $^{28}\text{Si}_{0.6}^{30}\text{Si}_{0.4}$  and  $^{29}\text{Si}$  bulk crystals at different incident laser (488 nm) power densities: 1.94, 0.97, 0.17, and 0.08  $\text{mW}/\mu\text{m}^2$ . (b) Evolution of average peak position and (c) evolution of average fwhm with incident laser power density for both  $^{28}\text{Si}_{0.6}^{30}\text{Si}_{0.4}$  and  $^{29}\text{Si}$  bulk samples extracted from the corresponding Voigt fits. In all of the three figures the data points for the  $^{28}\text{Si}_{0.6}^{30}\text{Si}_{0.4}$  bulk sample are shown in empty blue squares and that of  $^{29}\text{Si}$  bulk sample are shown in filled black circles. The averaging was done over measurements on four different spots on each sample. In (a), the red and the green curves correspond the Voigt fit of the respective raw data. In (b,c), the error bars in both the figures are smaller than the data symbols used. The dotted lines in both the figures are guide to the eye.

$$\text{fwhm}_{\text{Bulk}}(T = 300 \text{ K}) = \Delta_{\text{Anhrm}}^{\text{Iso-Mix Bulk}}(T = 300 \text{ K}) + \Delta_{\text{Isotope}}^{\text{Iso-Mix Bulk}} \quad (4)$$

In comparison, the fwhm of isotopically mixed  $^{28}\text{Si}_x^{30}\text{Si}_{1-x}$  NWs, after correcting for the spectral resolution, consists of three contributions

$$\text{fwhm}_{\text{Iso-Mix NW}} = \Delta_{\text{Anhrm}}^{\text{Iso-Mix NW}}(T = 300 \text{ K}) + \Delta_{\text{Isotope}}^{\text{Iso-Mix NW}} + \Delta_{\text{Surface}}^{\text{Iso-Mix NW}} \quad (5)$$

$\Delta_{\text{Surface}}^{\text{Iso-Mix NW}}$  is the broadening due to surface scattering of phonons. This contribution is peculiar to NWs but absent for bulk materials. Similarly for the fwhm of the isotopically pure  $^{29}\text{Si}$  NWs

$$\text{fwhm}_{\text{Si-29NW}} = \Delta_{\text{Anhrm}}^{\text{Si-29NW}}(T = 300 \text{ K}) + \Delta_{\text{Surface}}^{\text{Si-29NW}} \quad (6)$$

Next, we take  $\Delta_{\text{Anhrm}}^{\text{Iso-Mix Bulk}}|_T = \Delta_{\text{Anhrm}}^{\text{Iso-Mix NW}}|_T$  and  $\Delta_{\text{Isotope}}^{\text{Iso-Mix Bulk}} = \Delta_{\text{Isotope}}^{\text{Iso-Mix NW}}$ , because the anharmonic scattering and isotope scattering of phonons depend on the temperature and isotopic composition, but not on the size of the material as long as confinement effects are unimportant. Thus,  $\Delta_{\text{Isotope}}^{\text{Iso-Mix NW}} = 0.065 \text{ cm}^{-1}$  and at the lowest incident laser power density, corresponding to a temperature of about 300 K,  $\Delta_{\text{Anhrm}}^{\text{Iso-Mix NW}}$  is  $1.36 \text{ cm}^{-1}$ . We can now relate  $\Delta_{\text{Anhrm}}^{\text{Si-29 NW}}$  to  $\Delta_{\text{Anhrm}}^{\text{Iso-Mix NW}}$  through the inverse mass relation at a fixed temperature  $\Delta_{\text{Anhrm}}|_T \propto 1/\langle m \rangle$ , giving  $\Delta_{\text{Anhrm}}^{\text{Si-29 NW}}(T = 300 \text{ K}) \times \Delta_{\text{Anhrm}}^{\text{Iso-Mix NW}}(T = 300 \text{ K}) \times (\langle m \rangle_{\text{Iso-Mix}}/\langle m \rangle_{\text{Si-29}}) \approx 1.36 \text{ cm}^{-1}$ . Putting the value of the fwhm of  $^{29}\text{Si}$  NWs at the lowest incident power and  $\Delta_{\text{Anhrm}}^{\text{Si-29 NW}}$  in eq 6 we deduce the contribution of surface scattering to the NWs  $^{29}\text{Si}$ - $^{29}\text{Si}$  Raman peak broadening:  $\Delta_{\text{Surface}}^{\text{Si-29 NW}} = 0.88 \text{ cm}^{-1}$ . Note that the contribution of surface scattering of phonons, which is diameter dependent, is the same

382 for both types of NWs investigated in this work as they have  
 383 comparable diameters. It is therefore reasonable to conclude  
 384 that the surface induced broadening of Raman spectra is  
 385 the same for both types of NWs, that is  $\Delta_{\text{Surface}}^{\text{Iso-Mix NW}} \approx \Delta_{\text{Surface}}^{\text{Si-29 NW}} =$   
 386  $0.88 \text{ cm}^{-1}$ . Now, the left-hand side (LHS) of eq 5 at the lowest  
 387 incident laser power density is  $5.5 \text{ cm}^{-1}$ , whereas the right-hand  
 388 side (RHS) after summing up  $\Delta_{\text{Anhrm}}^{\text{Iso-Mix NW}}$ ,  $\Delta_{\text{Isotope}}^{\text{Iso-Mix NW}}$ , and  
 389  $\Delta_{\text{Surface}}^{\text{Iso-Mix NW}}$  equates to  $2.3 \text{ cm}^{-1}$ . The fact that the equality of  
 390 LHS and RHS in eq 5 does not hold suggests that there must  
 391 be some other source of spectral broadening that has not been  
 392 considered in eq 5. We rule out the possibilities of phonons  
 393 scattering at crystallographic defects because the two sets of  
 394 NWs are of high crystalline quality. This suggests that the  
 395 excess broadening is induced by effects other than those listed  
 396 above.

397 To verify the calculations above, we performed a series of  
 398 control experiments on isotopically mixed and isotopically pure  
 399 bulk samples. These isotopically engineered bulk crystals were  
 400 grown by floating zone technique. The secondary ion mass  
 401 spectrometer analysis (not shown here) estimated that the  
 402 isotopically mixed bulk sample is composed of about 60% of  
 403  $^{28}\text{Si}$  and 40% of  $^{30}\text{Si}$ . The spectra of both  $^{29}\text{Si}$  and  $^{28}\text{Si}_{0.6}^{30}\text{Si}_{0.4}$   
 404 bulk samples at four different laser power densities are shown in  
 405 Figure 4a. For these crystals, the average mass of the  
 406  $^{28}\text{Si}_{0.6}^{30}\text{Si}_{0.4}$  sample is slightly smaller than that of  $^{29}\text{Si}$  bulk  
 407 sample. Consequently, the spectra of the former are blueshifted  
 408 at all incident power as compared to the latter. The evolution of  
 409 the average peak position and the average fwhm with incident  
 410 laser power densities for both bulk samples are shown in Figure  
 411 4, panels band c, respectively. The data displayed in Figure 4b,c  
 412 were averaged over measurements on four different spots on  
 413 each sample. The  $^{28}\text{Si}_{0.6}^{30}\text{Si}_{0.4}$  and  $^{29}\text{Si}$  bulk sample have peaks  
 414 at  $514.9$  and  $512.3 \text{ cm}^{-1}$ , respectively. Unlike the case of Si  
 415 NWs, these phonon frequencies do not change significantly  
 416 with increasing laser power density. This is an expected  
 417 behavior because the effect of laser heating is ineffective in bulk  
 418 samples, which have higher thermal conductivities as compared  
 419 to NWs. The average fwhm, nearly  $3 \text{ cm}^{-1}$  smaller than those  
 420 measured for NWs, also shows a very limited increase with laser  
 421 power density that is almost identical for both bulk samples. It  
 422 is worth noting that the Si-Si mode of the  $^{28}\text{Si}_{0.6}^{30}\text{Si}_{0.4}$  bulk  
 423 sample is broader only by  $0.4 \text{ cm}^{-1}$  at the lowest incident laser  
 424 power than the Si-Si mode of  $^{29}\text{Si}$  bulk sample, which is  
 425 significantly less than the  $3.2 \text{ cm}^{-1}$  difference found between  
 426 the modes of the two sets of NWs. The difference of  $0.4 \text{ cm}^{-1}$   
 427 between the average fwhm of the two bulk samples at the  
 428 lowest laser power density is not entirely coming from isotope  
 429 scattering effect. Indeed, the average mass of  $^{28}\text{Si}_{0.6}^{30}\text{Si}_{0.4}$  being  
 430 smaller than the average mass of  $^{29}\text{Si}$ , the anharmonic scattering  
 431 of phonons, which scales inversely with average mass, is larger  
 432 in the  $^{28}\text{Si}_{0.6}^{30}\text{Si}_{0.4}$  bulk sample as compared to that of the  $^{29}\text{Si}$   
 433 bulk sample at a fixed temperature. The contribution of this  
 434 excess anharmonic phonon scattering to the Raman line width  
 435 is hidden within the difference of  $0.4 \text{ cm}^{-1}$  between the average  
 436 fwhm of the two bulk samples.

437 A plausible explanation of the observed broadening is the  
 438 nonuniform mixing of  $^{28}\text{Si}$  and  $^{30}\text{Si}$  isotopes during the VLS  
 439 growth of  $^{28}\text{Si}_x^{30}\text{Si}_{1-x}$  NWs. Indeed, the excess broadening of  
 440 the Raman spectra for the  $^{28}\text{Si}_x^{30}\text{Si}_{1-x}$  NWs probably originates  
 441 from the overlap of several narrower peaks corresponding to  
 442 different regions within a NW with different isotopic content.  
 443 For instance, in Figure 5a the Raman spectrum of a single  
 444  $^{28}\text{Si}_x^{30}\text{Si}_{1-x}$  NW recorded at the lowest laser power is

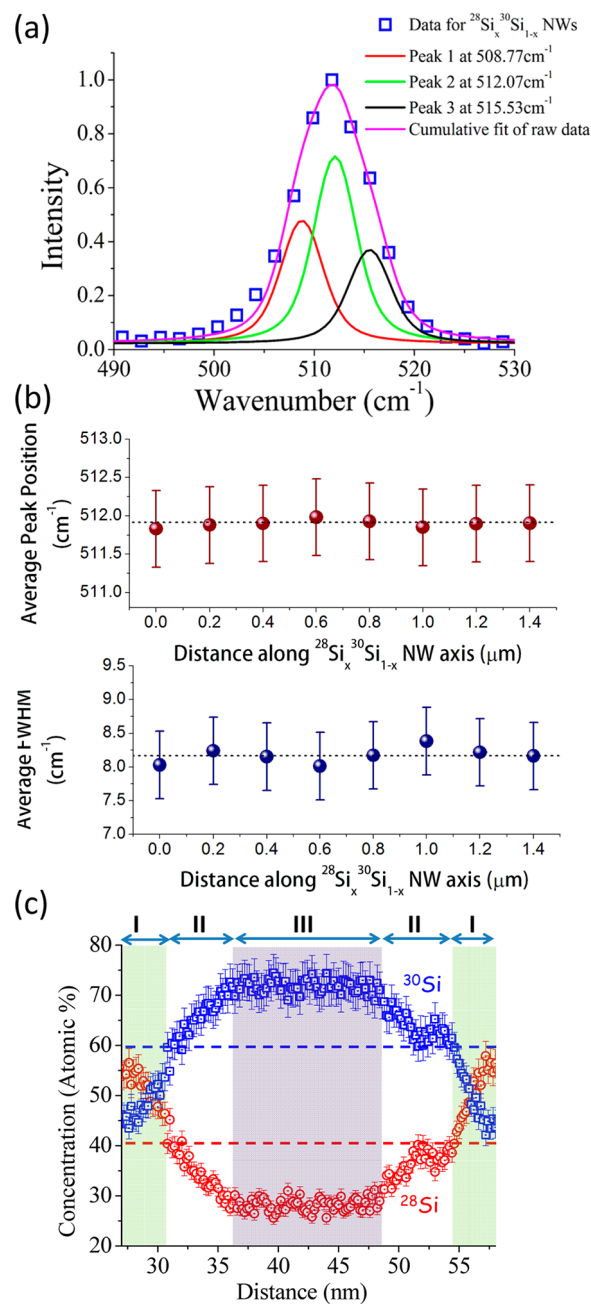


**Figure 5.** (a) The spectrum of a single  $^{28}\text{Si}_x^{30}\text{Si}_{1-x}$  NW at an incident power density of  $0.08 \text{ mW}/\mu\text{m}^2$ , data points shown in empty blue squares and the cumulative Voigt Fit (pink) has been simulated using the convolution of three different spectrum (red, green, and black) each representing different isotopic composition (details in text) within the NW; (b) peak position and fwhm profiles measured along the growth axis of single  $^{28}\text{Si}_x^{30}\text{Si}_{1-x}$  nanowires. Each data point is an average over a few measurements on different nanowires. The horizontal dashed lines indicate the average values; (c) APT radial profile of  $^{28}\text{Si}$  (red) and  $^{30}\text{Si}$  (blue) isotopes across the diameter of an isotopically mixed nanowire. The offset in x-axis reflects the thickness of the Ni protective layer deposited around the nanowire to prevent any damage that may occur during FIB processing.

deconvoluted in three different peaks corresponding to a  $^{28}\text{Si}$ -rich area, a  $^{30}\text{Si}$ -rich area, and a transition zone. Because the broadening due to isotopic scattering of phonons at  $300 \text{ K}$  is only  $0.065 \text{ cm}^{-1}$  the fwhm of each of the three peaks has been kept the same as that of an isotopically pure  $^{29}\text{Si}$  NW. Peak 1



450 (red) is at 508.77  $\text{cm}^{-1}$ , peak 2 (green) is at 512.07  $\text{cm}^{-1}$ , and  
451 peak 3 (black) is at 515.33  $\text{cm}^{-1}$ . The local compositions  
452 corresponding to these three peaks are 26.9, 45.8, and 65.3%,  
453 respectively. The estimated uncertainty from the spectral  
454 resolution of our Raman setup is about 7%.

455 Interestingly, Raman spectra recorded along the growth axis  
456 of individual  $^{28}\text{Si}_x^{30}\text{Si}_{1-x}$  NWs show that neither the peak  
457 position nor the fwhm of Si–Si mode vary along the nanowire  
458 growth axis (Figure 5b). This suggests that the isotopic content  
459 is uniform along the growth axis and thus the inferred  
460 nonuniformity of the isotopic content seems to be associated  
461 with the radial distribution of the two isotopes. To verify this  
462 intriguing observation, the nanowires investigated by Raman  
463 were also analyzed using atom probe tomography (APT),  
464 which is the only technique capable of providing the three-  
465 dimensional (3D) distribution of different isotopes in a  
466 nanoscale structure with a near atomic resolution. Details of  
467 the APT analysis will be reported elsewhere. Figure 5c displays  
468 the radial profiles of  $^{28}\text{Si}$  and  $^{30}\text{Si}$  isotopes across the diameter  
469 of an isotopically mixed nanowire. The average isotopic  
470 composition as estimated from APT  $^{28}\text{Si}_{0.41}^{30}\text{Si}_{0.59}$  which is  
471 close to the content obtained from Raman analysis  
472 ( $^{28}\text{Si}_{0.47}^{30}\text{Si}_{0.53}$ ). Importantly, we note that, as predicted from  
473 Raman spectra, APT analysis also confirms that the radial  
474 distribution of the two isotopes is not uniform, whereas their  
475 profiles along the growth axis (not shown here) remain  
476 unchanged also in agreement with Raman data (Figure 5b).  
477 Moreover, APT profiles demonstrate that the two isotopes are  
478 distributed in three different regions (Figure 5c):

479 (1) Near the surface where  $^{28}\text{Si}$  ( $^{30}\text{Si}$ ) content is higher  
480 (lower) than its average content in the entire nanowire (region  
481 I). The width of this region is about 26.3% of the nanowire  
482 diameter.

483 (2) At the core of the nanowire where  $^{30}\text{Si}$  ( $^{28}\text{Si}$ ) content is  
484 higher (lower) than its average content in the entire nanowire  
485 (region III). The width of this region is about 34.3% of the  
486 nanowire diameter.

487 (3) A transition region between the two regions I and III  
488 where the content of  $^{30}\text{Si}$  ( $^{28}\text{Si}$ ) increases (decreases)  
489 monotonically inward from nanowire surface to its core. The  
490 width of this region is about 39.4% of the nanowire diameter.

491 The average isotopic composition of each region is  $x$  (I) =  
492  $0.50 \pm 0.01$  ( $^{28}\text{Si}_{0.5}^{30}\text{Si}_{0.5}$ );  $x$  (II) =  $0.35 \pm 0.01$  ( $^{28}\text{Si}_{0.35}^{30}\text{Si}_{0.65}$ );  
493 and  $x$  (III) =  $0.75 \pm 0.01$  ( $^{28}\text{Si}_{0.25}^{30}\text{Si}_{0.75}$ ). Clearly, APT analysis  
494 confirms Raman-based observations reported above. At the  
495 same time, the 3D atom-by-atom distribution of each isotope  
496 within a single nanowire also raises fundamental questions  
497 about the basic mechanisms and dynamics of the VLS growth.  
498 Addressing these very important questions extends beyond the  
499 main focus of this Letter.

500 In summary, we have demonstrated the growth of isotopi-  
501 cally mixed Si NWs via the VLS process using isotopically  
502 enriched silane precursors  $^{28}\text{SiH}_4$ ,  $^{29}\text{SiH}_4$ , and  $^{30}\text{SiH}_4$ . Using  
503 Raman spectroscopy, the vibrational properties of these NWs  
504 were investigated and compared to that of isotopically pure  $^{29}\text{Si}$   
505 NWs having a close reduced mass. The outcome of the  
506 comparative study indicates that there is an enhanced phonon  
507 scattering in isotopically mixed NWs, which manifests itself at  
508 two interrelated levels. First, the measured Raman spectra of  
509 the  $^{28}\text{Si}_x^{30}\text{Si}_{1-x}$  NWs were found to react to laser power quite  
510 differently from those of  $^{29}\text{Si}$  NWs. The redshift in peak  
511 position and broadening of Raman spectra are more significant  
512 for the former as compared to the latter with the local

temperature of the  $^{28}\text{Si}_x^{30}\text{Si}_{1-x}$  NWs at the highest power 513  
density being almost 120 K above that of the  $^{29}\text{Si}$  NWs. On the 514  
basis of Raman nanothermometry, we estimated  $\sim 30\%$  515  
reduction in the thermal conductivity of the  $^{28}\text{Si}_x^{30}\text{Si}_{1-x}$  NWs 516  
as compared to that of the  $^{29}\text{Si}$  NWs around 300 K. Second, the 517  
fwhm of the  $^{28}\text{Si}_x^{30}\text{Si}_{1-x}$  NWs was found to be significantly 518  
larger than that of  $^{29}\text{Si}$  NWs regardless of the laser power. We 519  
showed that this cannot come entirely from the isotope effect 520  
and that the origin of this excess broadening might lie in 521  
nonuniformity in mixing of the two isotope atoms within a 522  
 $^{28}\text{Si}_x^{30}\text{Si}_{1-x}$  NW. This nonuniform mixing of  $^{28}\text{Si}$  and  $^{30}\text{Si}$  may 523  
unravel new insights into the dynamics of the VLS growth, 524  
which extends beyond the scope of the current work. The work 525  
presented here provides an essential body of information for 526  
devices looking to exploit the thermal properties of NWs. The 527  
results clearly show that the isotopically disordered and the 528  
isotopically pure NWs respond to laser heating almost similarly 529  
at low power ranges but their behavior differ drastically at high 530  
power range. For NW-based devices, the isotopically mixed 531  
NWs can be exploited for applications requiring lower thermal 532  
conductivity, whereas the isotopically pure NWs are ideal for a 533  
more efficient dissipation of heat. 534

## ■ ASSOCIATED CONTENT

 535

### 📄 Supporting Information

 536

Additional information including experimental details, addi- 537  
tional figures, and additional references. The Supporting 538  
Information is available free of charge on the ACS Publications 539  
website at DOI: 10.1021/acs.nanolett.5b00708. 540

## ■ AUTHOR INFORMATION

 541

### Corresponding Author

 542

\*E-mail: oussama.moutanabbir@polymtl.ca. 543

### Notes

 544

The authors declare no competing financial interest. 545

## ■ ACKNOWLEDGMENTS

 546

O.M. acknowledges funding from NSERC-Canada (Discovery 547  
Grants) and Canada Research Chair, Fondation de l'École 548  
Polytechnique de Montréal. The work at Keio was supported in 549  
part by the Grant-in-Aid for Scientific Research by MEXT, in 550  
part by NanoQuine, in part by FIRST, and in part by JSPS 551  
Core-to-Core Program. J.A. acknowledges the funding from the 552  
Generalitat de Catalunya 2014 SGR 1638. M.d.I.M. thanks the 553  
CSIC Jae-Predoc program. J.A. and M.d.I.M. thank funding 554  
from Spanish MINECO MAT2014-51480-ERC. The micros- 555  
copy works have been conducted in the "Laboratorio de 556  
Microscopias Avanzadas" at "Instituto de Nanociencia de 557  
Aragon - Universidad de Zaragoza". Authors acknowledge the 558  
LMA-INA for offering access to their instruments and expertise, 559  
especially to Dr. Cesar Magen. 560

## ■ REFERENCES

 561

- (1) Cardona, M.; Thewalt, M. L. W. *Rev. Modern Phys.* **2005**, *77*, 562  
1173–1224. 563
- (2) Haller, E. E. *MRS Bull.* **2006**, *31*, 547–553. 564
- (3) Hu, M.; Sinn, H.; Alatas, A.; Sturhahn, W.; Alp, E.; Wille, H.; 565  
Shvyd'ko, Y.; Sutter, J.; Bandaru, J.; Haller, E.; Ozhogin, V.; Rodriguez, 566  
S.; Colella, R.; Kartheuser, E.; Villeret, M. *Phys. Rev. B* **2003**, *67*, 567  
113306. 568
- (4) Davies, G.; Lightowlers, E. C.; Itoh, K.; Hansen, W. L.; Haller, E. 569  
E.; Ozhogin, V. *Semicond. Sci. Technol.* **1992**, *7*, 1271–1273. 570

571 (5) Tyryshkin, A. M.; Tojo, S.; Morton, J. J.; Riemann, H.;  
572 Abrosimov, N. V.; Becker, P.; Pohl, H. J.; Schenkel, T.; Thewalt, M. L.;  
573 Itoh, K. M.; Lyon, S. A. *Nat. Mater.* **2012**, *11*, 143–147.  
574 (6) McCamey, D. R.; Van Tol, J.; Morley, G. W.; Boehme, C. *Science*  
575 **2010**, *330*, 1652–1656.  
576 (7) Simmons, S.; Brown, R. M.; Riemann, H.; Abrosimov, N. V.;  
577 Becker, P.; Pohl, H. J.; Thewalt, M. L. W.; Itoh, K. M.; Morton, J. J. *L.*  
578 *Nature* **2011**, *470*, 69–72.  
579 (8) Itoh, K. M. *Solid State Commun.* **2005**, *133*, 747–752.  
580 (9) Ozhogin, V. I.; Inyushkin, A. V.; Taldenkov, A. N.; Tikhomirov,  
581 A. V.; Popov, G. É.; Haller, E.; Itoh, K. *J. Exp. Theor. Phys. Lett.* **1996**,  
582 *63*, 490–494.  
583 (10) Kremer, R. K.; Graf, K.; Cardona, M.; Devyatkykh, G. G.; Gusev,  
584 A. V.; Gibin, A. M.; Inyushkin, A. V.; Taldenkov, A. N.; Pohl, H. J.  
585 *Solid State Commun.* **2004**, *131*, 499–503.  
586 (11) Bracht, H.; Eon, S.; Frieling, R.; Plech, A.; Issenmann, D.; Wolf,  
587 D.; Lundsgaard Hansen, J.; Nylandsted Larsen, A.; Ager, J. W., III;  
588 Haller, E. E. *New J. Phys.* **2014**, *16*, 015021.  
589 (12) Nakajima, M.; Harima, H.; Morita, K.; Itoh, K.; Mizoguchi, K.;  
590 Haller, E. *Phys. Rev. B* **2001**, *63*, 161304.  
591 (13) Morelli, D.; Heremans, J.; Slack, G. *Phys. Rev. B* **2002**, *66*,  
592 195304.  
593 (14) Yang, N.; Zhang, G.; Li, B. *Nano Lett.* **2008**, *8*, 276–280.  
594 (15) Hattori, J.; Uno, S. *Jpn. J. Appl. Phys.* **2013**, *52*, 04CN04.  
595 (16) Moutanabbir, O.; Senz, S.; Zhang, Z.; Gösele, U. *Nano Today*  
596 **2009**, *4*, 393–398.  
597 (17) Hannon, J. B.; Kodambaka, S.; Ross, F. M.; Tromp, R. M.  
598 *Nature* **2006**, *440*, 69–71.  
599 (18) Bailly, A.; Barrett, N.; Zagonel, L. F.; Gentile, P.; Pauc, N.;  
600 Dhalluin, F.; Baron, T.; Chabli, A.; Cezar, J. C.; Brookes, N. B.; R, O.  
601 *Nano Lett.* **2008**, *8*, 3709–3714.  
602 (19) Adu, K.; Gutiérrez, H.; Kim, U.; Eklund, P. *Phys. Rev. B* **2006**,  
603 *73*, 155333.  
604 (20) Moutanabbir, O.; Miyamoto, S.; Haller, E. E.; Itoh, K. M. *Phys.*  
605 *Rev. Lett.* **2010**, *105*, 026101.  
606 (21) Balkanski, M.; Wallis, R.; Haro, E. *Phys. Rev. B* **1983**, *28*, 1928–  
607 1934.  
608 (22) Scheel, H.; Reich, S.; Ferrari, A. C.; Cantoro, M.; Colli, A.;  
609 Thomsen, C. *Appl. Phys. Lett.* **2006**, *88*, 233114.  
610 (23) Soini, M.; Zardo, I.; Uccelli, E.; Funk, S.; Koblmüller, G.;  
611 Fontcuberta i Morral, A.; Abstreiter, G. *Appl. Phys. Lett.* **2010**, *97*,  
612 263107.  
613 (24) Frieling, R.; Radek, M.; Eon, S.; Bracht, H.; Wolf, D. E. *Appl.*  
614 *Phys. Lett.* **2014**, *105*, 132104.  
615 (25) Chen, S.; Wu, Q.; Mishra, C.; Kang, J.; Zhang, H.; Cho, K.; Cai,  
616 W.; Balandin, A. A.; Ruoff, R. S. *Nat. Mater.* **2012**, *11*, 203–207.  
617 (26) Widulle, F.; Ruf, T.; Konuma, M.; Silier, I.; Cardona, M.;  
618 Kriegseis, W.; Ozhogin, V. I. *Solid State Commun.* **2001**, *118*, 1–22.  
619 (27) Piscanec, S.; Ferrari, A. C.; Cantoro, M.; Hofmann, S.; Zapien, J.  
620 A.; Lifshitz, Y.; Lee, S. T.; Robertson, J. *Mater. Sci. Eng., C* **2003**, *23*,  
621 931–934.  
622 (28) Fuchs, H. D.; Grein, C. H.; Cardona, M.; Hansen, W. L.; Itoh,  
623 K.; Haller, E. E. *Solid State Commun.* **1992**, *82*, 225–228.  
624 (29) Kittel, C. *Introduction to Solid State Physics*, 8th ed.; Wiley: New  
625 York, 2004.  
626 (30) Callaway, J. *Phys. Rev. Lett.* **1959**, *113*, 1046–1051.  
627 (31) Gupta, R.; Xiong, Q.; Adu, C. K.; Kim, U. J.; Eklund, P. C. *Nano*  
628 *Lett.* **2003**, *3*, 627–631.  
629 (32) From ref 26,  $\Delta_{\text{Anhrm}}^{\text{Nat-Si Bulk}} (T = 6 \text{ K}) \approx 1.21 \text{ cm}^{-1}$  and  $\Delta_{\text{Isotope}}^{\text{Nat-Si Bulk}}$   
630 is negligible. This makes the anharmonic contribution equal to the  
631 total line broadening from bulk  $^{\text{Nat}}\text{Si}$  sample. The anharmonic  
632 contribution was extrapolated to 300 K using eq 3, giving  $\Delta_{\text{Anhrm}}^{\text{Nat-Si Bulk}}$   
633  $(T = 300 \text{ K} \approx \text{fwhm}^{\text{Nat-Si}} (T = 300 \text{ K}) \approx 2.154 \text{ cm}^{-1}$ . Next, a  $^{\text{Nat}}\text{Si}$  bulk  
634 sample was measured using the InVia RM 3000 setup using 488 nm at  
635 an incident power density of  $0.08 \text{ mW}/\mu\text{m}^2$  and the fwhm was found  
636 to be  $\sim 5 \text{ cm}^{-1}$ . We attributed this excess line broadening ( $\sim 3 \text{ cm}^{-1}$ ) of  
637 InVia RM 3000 setup to instrumental resolution. We did not calculate  
638 the contribution of instrumental broadening for the other setup (used  
639 for high power measurements) because the entire analysis concerning

the fwhm of the NWs was done using the data at the lowest recorded 640  
power density which was recorded using the InVia RM 3000 setup. 641  
(33) Moutanabbir, O.; Isheim, D.; Seidman, D. N.; Kawamura, Y.; 642  
Itoh, K. M. *Appl. Phys. Lett.* **2011**, *98*, 013111. 643